scientific reports

Check for updates

OPEN

Explainable analysis of the complex maze magnetic domain structure through extension of the Landau free energy model by adding an entropy feature

K. Masuzawa[1], A. L. Foggiatto[1], S. Kunii[1], R. Nagaoka[1], M. Taniwaki[1], T. Yamazaki[1], C. Mitsumata[1,2], I. Obayashi[3], Y. Hiraoka[4] & M. Kotsugi[1]✉

Maze magnetic domains exhibit complex, temperature-dependent behavior that impacts energy loss in soft magnets, yet their magnetization reversal mechanisms remain poorly understood due to current model limitations. To address this gap, we develop an entropy-extended Landau free energy model that incorporates thermal effects into the analysis of magnetic domain. We employ a data-driven pipeline combining persistent homology, energy decomposition, and principal component analysis to construct an interpretable model that quantifies structure–property relationships and enables causal analysis of magnetic pattern formation. Using this approach, we trace entropy increases to their origins in initial domain configurations and quantify energy transfer among entropic, demagnetization, and exchange contributions. We also find that domain wall lengthening tracks increasing structural complexity, yielding previously inaccessible insights into magnetization reversal mechanism and enabling automated visualization. Our entropy-augmented model provides an explainable framework to decipher magnetization processes and guide the design of magnetic materials to reduce energy loss.

With increases in electricity demands worldwide and the rapid increase in the use of electric vehicles, improving motor energy conversion efficiency has become a critical issue. Notably, iron loss accounts for 31% of motor energy loss, with most of this energy dissipated as heat[1–3]. In applications, motors operate in high-temperature environments, and thermal demagnetization causes serious problems such as increased coercivity, iron loss, and Joule heating due to eddy currents[1–10]. The inner area of the hysteresis loop is a simple parameter representing energy consumption in the magnetization reversal process, such as energy-related iron loss. Understanding the magnetic domain structure is equally important, because domain configurations and domain wall propagation directly influence macroscopic magnetic properties like coercivity and hysteresis loss. However, analysis of the magnetic domain structure is challenging because of the complex interplay of multiple factors, including the metallographic structure, thermal effect, and energy stability[7–25]. Thermal agitation reshapes domain morphology—inducing nucleation, branching, stripe thinning, and enhanced zig-zagging—so maze patterns vary with field and temperature. Yet how this evolving complexity and entropy translate into energy loss remains unclear, constraining strategies for loss minimization.

In applied soft magnets for motors, the thermal contribution to the magnetization reversal is therefore pivotal: higher temperatures shift nucleation thresholds and alter domain-wall propagation and branching, reconfiguring the reversal pathway. The magnetic domain microstructure of a soft magnetic material is determined by the delicate balance among the demagnetization effect, domain walls and entropy. Magnetic domains show various fine structures, such as the maze domain structure, the pinning domain wall, the lancet domain, and the Barkhausen jump[16,20,23,26–30]. Maze domains are intricate zig-zag patterns typical of perpendicularly magnetized films. Furthermore, the microstructure changes in a complex and abrupt manner in response to an external magnetic field[9]. Fundamentally, the thermal effect induces fluctuations in magnetic

[1]Department of Material Science and Technology, Tokyo University of Science, 6-3-1, Niijuku, Katsushika, Tokyo 125-8585, Japan. [2]Graduate School of Pure and Applied Science, University of Tsukuba, 1-1-1 Tennodai, Tsukuba 305-8577, Japan. [3]Interdisciplinary Education and Research Field, Okayama University, 2-1-1, Tsushimanaka, Kita-ku, Okayama 700-8530, Japan. [4]Kyoto University Institute for Advanced Study, Kyoto University, Yoshida Ushinomiya-cho, Sakyo-ku, Kyoto 606-8501, Japan. ✉email: kotsugi@rs.tus.ac.jp

moments, leading to complex changes in the magnetic domain microstructure[7,9,11,13,14,31–33]. As temperature rises, maze domains develop increased branching and more jagged, zig-zag walls underscoring how thermal fluctuations complexify the domain morphology. Under an applied field, reverse domains nucleate, grow, branch, and shrink, culminating in a flip of the magnetization. These microscopic transformations collectively produce the macroscopic hysteresis loop and its associated energy loss. However, clarifying the complex mechanisms of magnetization reversal, namely, which physical effects play key roles and how the microstructure affects energy loss, remains a great challenge. A comprehensive analysis method linking the complex microstructure, energy, and entropy has not yet been fully established.

Regarding previous analyses of magnetic domains, various computational simulations have been performed. With Ginzburg–Landau (GL) theory, which is based on thermal statistical mechanics, thermal contributions to magnetic moments can be considered, and magnetization reversal can be simulated via the Kronmüller model (simultaneous rotation model). GL theory, originally developed for superconductivity, has since been adapted to reproduce complex Turing patterns—including maze magnetic domain—highlighting its broad applicability[34–36]. However, the mean-field approximation used in GL theory assumes spatial homogeneity, limiting its accuracy in treating microstructural details[8,13,19,37]. Conversely, the Landau–Lifshitz–Gilbert (LLG) equation effectively and accurately handles inhomogeneous magnetic domains, with success in nanomagnetics and spintronics[15,17,22,24,25,27–29], enabling accurate simulations of domain wall dynamics in nanoscale magnetic devices. However, this approach does not satisfactorily consider thermal effects; temperature-driven fluctuations are often not taken into account. Therefore, neither the GL nor LLG framework alone can fully address magnetization reversal in real, inhomogeneous materials. This gap has motivated researchers to leverage experimental observations and data-driven analysis to gain further insights.

Various experimental techniques, including synchrotron radiation and Kerr microscopy, have been efficiently used to capture large datasets of magnetic domains under various external fields and temperatures[11,12,14,16,32,34,35,38–46]. These methods have yielded notable results for nanomagnetic materials and permanent magnets. Kerr microscopy has visually captured thermally assisted nucleation, branching, stripe thinning, and zig-zag maze formation across coercivity, enabling frame-by-frame inspection of wall dynamics. Soft X-ray magnetic microscopies provide element-specific views of maze/stripe domain textures with tens-of-nanometer spatial resolution, enabling a correlation analysis with film parameters. However, performing quantitative causal analysis –determining how specific microscopic domain features cause particular macroscopic effects– from such visual data is notoriously difficult. Microstructural features lack standardization, and manual choices—thresholds and region selection—make branching frequency, stripe width, wall curvature, and zig-zag amplitude observer-dependent and condition-sensitive. Field and temperature co-vary, adding confounding and path dependence. Each of the above analytical methods has strengths and limitations. The core issue is the lack of a robust approach to effectively analyse complex magnetization reversal mechanisms driven by thermal and spatial fluctuations in the magnetization, which is a critical issue in both fundamental magnetism and its applications. In other words, conventional simulations oversimplify real materials, while experiments reveal complexity without a clear way to quantify cause and effect – underscoring the need for an improved analytical approach.

In this study, we introduce the entropy-feature-eXtended Ginzburg-Landau (eX-GL) model[47–49]. This is a physics-based explainable artificial intelligence (XAI) framework, designed to mechanistically explain the temperature-dependent magnetization reversal process. The model's explanatory power is rooted in the use of free energy as the central quantity linking microscopic domain morphology to macroscopic magnetic behavior. The core of the model is the explicit integration of the entropy term TS into the Helmholtz free energy F, allowing thermal fluctuations to be analyzed on an equal footing with demagnetization and exchange. This integrated approach bridges a critical gap, overcoming the respective limitations of conventional Ginzburg-Landau theory (oversimplified microstructure), Landau-Lifshitz-Gilbert simulations (limited treatment of thermal effects), and advanced microscopy (difficulty in causal quantification).

Our data-driven pipeline translates this physical model into a quantitative analysis. We employ persistent homology (PH) to transform complex domain textures into a robust structural feature, which serves as a surrogate order parameter. By constructing an energy landscape in this feature space and decomposing its gradients, we perform a causal analysis that reveals which physical terms drive or resist specific structural transformations. We identify data points with steep energy gradients as 'outliers' corresponding to significant energy barriers. Visualizing their associated microstructures reveals the spatial origins of entropy increases and the underlying reversal mechanisms. Extending our previously validated framework for static coercivity[47–53], this study applies the eX-GL model to the complex maze magnetic domains in a rare-earth iron garnet (RIG) system, quantifying the energy transfer among the entropic, demagnetization, and exchange contributions. For the first time, it also visualizes how the increasing structural complexity of these domains originates from a robust coupling between entropy and the lengthening of domain walls. This discovery provides a direct, mechanistic link between configurational entropy and domain wall proliferation, a key pathway for energy loss in soft magnetic materials.

Results

Workflow of the eX-GL model development

We designed an eX-GL model of maze magnetic domains that incorporates thermal effects (Fig. 1). We focus on analysing the magnetic free energy within a data-driven framework to elucidate the magnetization reversal mechanism. The magnetic domain structure is analysed using persistent homology (PH), and the obtained features are correlated with the free energy. We draw the free energy landscape in data space to robustly link the structure and various functions. To make this link explicit, we embed the PH-derived features in a low-dimensional space and analyze free-energy gradients along those axes. Specifically, we perform energy decomposition and causal analysis to quantitatively elucidate how the energy barriers behave in response to the

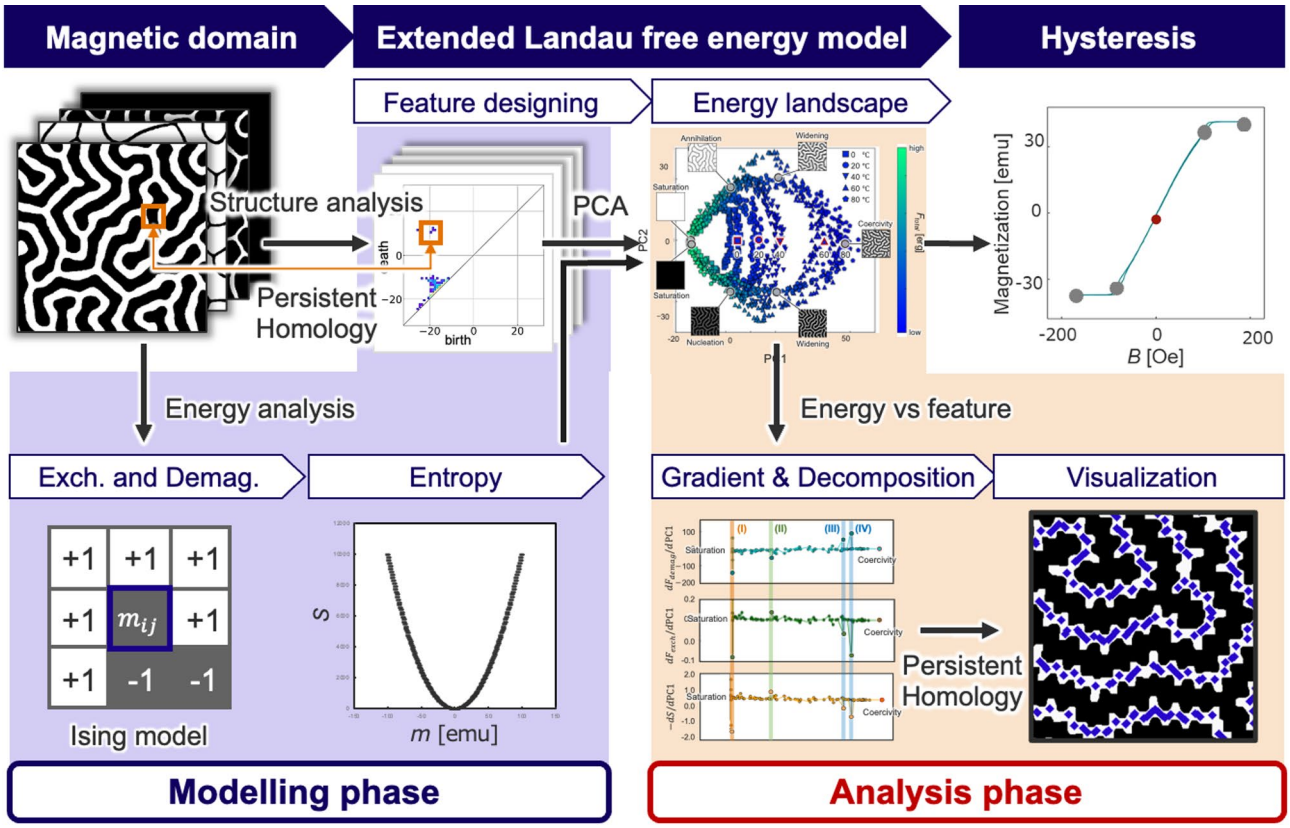

Fig. 1. Workflow of eX-GL analysis. In the modelling phase (left panel), we input the magnetic domain structure into the model and use persistent homology to extract structural features. We also calculate the free energy, including the entropy term, from image data. By integrating the obtained features, we construct a novel energy landscape in data space, which enables robust connections between microscopic microstructures and macroscopic functions across hierarchies. In the analysis phase (right panel), we examine the correlation between the structural features and free energy. In particular, we introduce a simple variable transformation that preserves consistency with conventional Landau theory while enabling detailed analysis. We then decompose the free energy into physically interpretable components to permit causal examination of the underlying mechanisms. The resulting features allow us to visualize how functional behaviour arises from the initial magnetic domain structure.

external magnetic field and which physical effects contribute to structural changes in the magnetization reversal process. Furthermore, we extract the energy barriers as features and visualize the factors contributing to entropy by tracing them back to the original magnetic domain structure.

In the first step of the eX-GL workflow (the modelling phase, left panel), we use persistent homology (PH) to extract the inhomogeneity in the maze magnetic domain structure as a feature[54–57]. PH, which is an advanced topological concept, quantifies the shape and connections within fine structures. Recently, PH has been applied to polymers and structural materials[49,54,57–59], and in this study, we use PH to characterize the spatial distribution of the magnetization within domain images.

The magnetic free energy is analysed in terms of the exchange energy, demagnetization energy, and entropy components to facilitate a detailed causal analysis of the underlying physical phenomena, with a particular focus on the entropy term. For the entropy calculation, rare-earth iron garnet (RIG) can be taken as a typical/model soft magnetic material. RIG exhibits the maze magnetic domain structure, which is known to undergo complex changes depending on the temperature and magnetic field[7,9,11,14,31,33]. RIG can be well approximated by the Ising model of North and South poles, as its binary magnetization states allow the stochastic formation of domain structures to be expressed by a binomial distribution. Although the exact magnetization reversal probability is not 1/2, the small volume of the domain walls relative to the observation field, along with the random positions of the magnetic walls, justifies this approximation. With over 10^5 pixels per image, the central-limit theorem justifies a Gaussian approximation. Additionally, both the demagnetization and exchange energies can be analysed via the Ising model, as in previous studies[60,61].

Next, pattern recognition, a machine learning technique, is used to extract essential features of structural changes[62], enabling the construction of a novel energy landscape in data space. The model leverages these structural features to analyse the free energy landscape. We establish quantitative links between structural features and physical parameters, building on prior analyses of defect pinning in Permalloy and energy loss in non-oriented electrical steel[47,48,63]. Simple variable transformations maintain consistency with conventional

Landau theory while robustly connecting the structure and free energy[19,47–53]. The use of an interpretable machine learning technique enables quantitative evaluation of the energy costs associated with microstructural changes. This approach is intended to facilitated integrated analysis of microstructural details, which are challenging to consider in GL calculations, and thermal contributions, which are cumbersome to consider in LLG calculations. Additionally, this approach enables the origin of macroscopic functions to be traced to the initial microstructural magnetic domains, facilitating automated function analysis and extraction of previously inaccessible information.

In the analysis phase (right panel), we focus on examining the energy landscape. The key idea is to explore the relationship between the distance between data points in data space and energy to link microscopic magnetic domain structures to the macroscopic magnetization reversal process. This method exploits the feature vector representation of the magnetic domain structure and the preservation of the Euclidean distance in latent space. This approach is conceptually aligned with conventional Landau theory, linking the energy landscape in feature space with the notion of coercivity. In conventional Landau theory, the coercivity is defined as the effective magnetic field H_{eff} derived by differentiating the free energy F with respect to the order parameter, i.e., the magnetization M. In other words, the effective field is the gradient of the energy landscape. In extended Landau theory, we use principal component (PC) of structure features for variable transformation, allowing us to redefine the energy landscape gradient (the effective field in conventional Landau theory), as shown in Eq. (1).

$$H_{eff} = -\frac{\partial F}{\partial M} = -\frac{\partial F}{\partial PC}\frac{\partial PC}{\partial M} \tag{1}$$

The first term on the right-hand side represents the energy gradient in feature space and can be used to analyse the energy cost associated with structural changes. This energy gradient can be used to detect notable energy barriers contributing to macroscopic functions, which can then be decomposed to analyse relationships among energy components, enabling a quantitative discussion of the underlying phenomena. By examining the energy interactions among these components, we can clarify causal relationships among physical phenomena. Additionally, energy barriers can be converted into features, and the contributing factors can be visualized and traced back to the initial image, allowing us to identify the origin of energy loss with respect to the initial magnetic domains. The second term can be easily obtained by correlating the feature with the magnetization. In the extended GL model, the order parameter is redefined as a structural feature, allowing analysis of energy costs related to structural changes and linking of the structure and functions across material hierarchies.

We systematically developed the eX-GL framework in previous works. The fundamental principles of this model were established using computational data[47,50] and further developed through both computational and experimental approaches[48]. We also developed an experimental eX-GL model using Kerr microscope data of maze magnetic domain under constant-temperature conditions[60]. Theoretical extensions from the Kronmüller model to coercivity theory have also been demonstrated[13,47,48,53,60]. Additionally, we analysed the magnetization reversal process in polycrystalline magnetic materials, including the contribution of the grain boundaries[48,52]. This magnetization reversal process corresponds to the minimal energy pathway on the energy landscape, with energy losses and the coercivity analysed through energy gradients leading to saddle points[9,19,47–50,53] Including the entropy term deepens understanding of the complex magnetization reversal process and reveals previously hidden insights.

Magnetic domain structure measurement

We obtained magnetic domain structures of rare-earth iron garnet (RIG), a prototypical material that naturally hosts maze domains, and therefore used it as the model system in this study. To assess the temperature dependence of the magnetization reversal process, the magnetic domain structure of a RIG sample (film thickness of 475 μm) at temperatures of 0, 20, 40, 60, and 80 °C was analysed with a polar Kerr microscope (Fig. 2a), with the external magnetic field and temperature dependencies recorded as a movie (Additional Information). The magnetic domain structure with perpendicular magnetization was obtained using a polar Kerr configuration. The imaging area was 800 μm × 800 μm (512 × 512 pixels). The external magnetic field was quasistatically varied from 200 Oe to -200 Oe in 2 Oe step increments. Sequential magnetic domain structure measurements were performed, yielding 400 data points per hysteresis loop. A total of 2000 data points was collected. The saturation magnetization was 3.2×10^3 emu/cc. The domain image was binarized using Otsu's method (see the Methods section for details).

The experimental results demonstrated clear contrast and continuous changes in the out-of-plane magnetic domain structure with the external magnetic field and temperature. The white (black) pixels correspond to up (down) magnetization. A movie of the magnetic domains is provided in the Additional Information. Visual inspection reveals that, beginning from a fully black saturated state (-200 Oe), small nuclei of white reversal domains start to form (Supplemental Movie). These nuclei act as starting points for the elongation of stripe reversal domains, which create microstructures as they connect and branch with nearby nuclei. After the stripes stop elongating, the reversal domains widen. This behaviour increases the complexity of the domain structure, which forms a maze pattern at the coercivity. Beyond the coercivity point, the reversal domains continue to expand, with the black domains narrowing. The black domains shrink into stripes, which eventually break apart and disappear. Finally, the black domains become dots, and the system fully saturates, becoming a white domain. Thus, the results suggest that the complexity of the magnetic domain structure increases with increasing temperature (Fig. 2a). However, quantifying the complexity in these visualizations is challenging. The behaviour during the formation of the maze magnetic domain aligns well with previous studies[7,11,12,14].

To quantify this complexity, we characterized the magnetic domain structure using PH. The resulting persistence diagrams (PDs) serve as topological descriptors of the images. PH extends the mathematical concept of topology to discrete structural data, enabling the description of shape information such as the size,

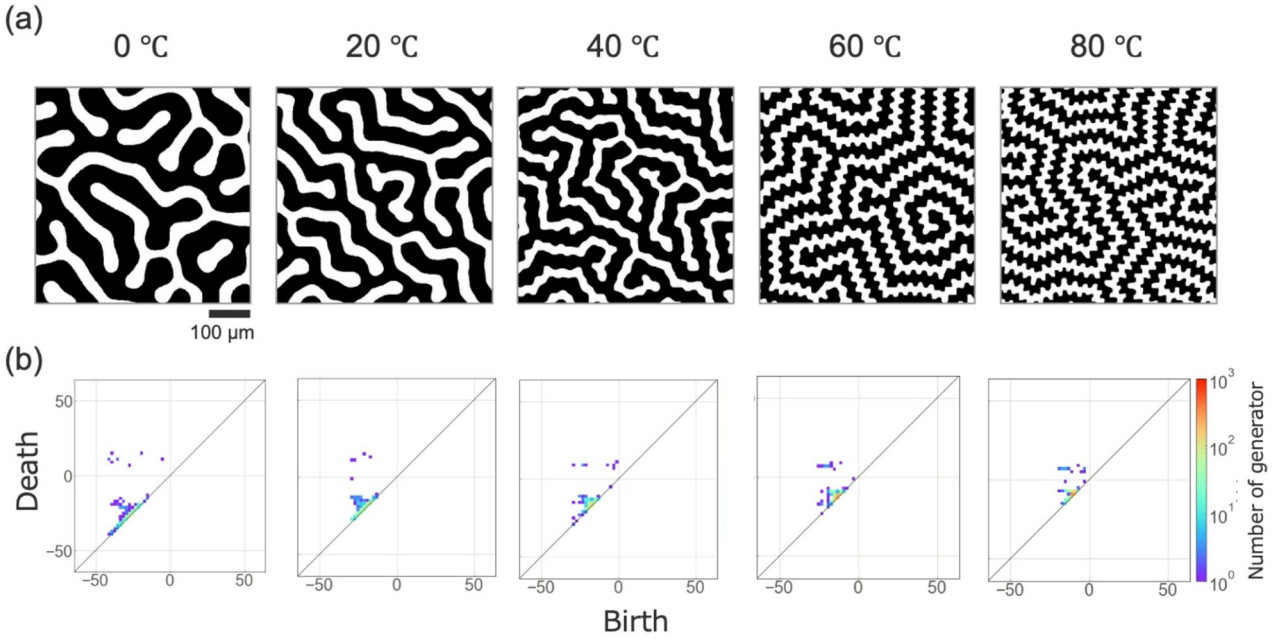

Fig. 2. Maze magnetic domain structures and persistence diagrams. (**a**) Maze-like magnetic domain structures in a RIG single-crystalline thin film observed via Kerr microscopy. The external magnetic field was swept from − 200 to 200 Oe along the z-axis, and the temperature was varied from 0 to 80 °C. The magnetic domain structures near the coercivity field are shown as representative data. The complex behaviour of the maze domain structure, which varies with the external field and temperature, can be observed. The complete movies can be seen in the Additional Information. (**b**) Persistence diagrams (PDs) of the microstructural features of the magnetic domain structure extracted using persistent homology. Near-diagonal generators in the persistence diagram indicate stripe and smooth textures, whereas generators far from the diagonal reflect curved or necked zig-zag structures. Generators near the lower-left corner signal thicker textures, while those toward the upper-right indicate thinner ones.

distortion and connectivity of holes[49,56–59]. The microstructure can be analysed via a process called "filtration". The Manhattan distance is used to analyse the boundary between white and black pixels. The boundary is then expanded or contracted by continuously varying the white–black threshold. During this process, the thresholds *b* (birth) at which a "hole" is created and *d* (death) at which it vanishes are recorded to extract the structural features. The pair (*b*, *d*) is referred to as a generator and provides information characterizing the shape of the hole. By processing the thresholds across the entire image, the PD is constructed. This approach effectively condenses structural information into the PD, making it a useful metric for capturing the essential features of a material's structure. In the present study, the 0th-order PDs were obtained (Fig. 2b and supplemental movie). The 0th-order PD focuses on the black magnetic regions and can be used to track their connectivity. When there are no generators in the PD, the black magnetic domain fully occupies the area. If generators are sparsely distributed away from the diagonal, the black domain is being eroded by white reversal domains, resulting in the formation of a microstructure. As the maze-like zig-zag patterns are progressively thinned, the generators in the PD shift progressively upward along the diagonal, reflecting concurrent reductions in their birth and death scales. The PD represents the maze-like microstructure of the magnetic domains. As the magnetic domain structure changes and the black domains continue to shrink, the generators in the PD shift towards the upper right and eventually disappear, indicating that the black domains are fully engulfed by the white domains, leading to complete magnetization reversal. The continuous change in the PD confirms that the proposed method successfully captures the gradual change in the domain structure, a capability made possible by the inclusion of an entropy term in the analysis. Moreover, this behaviour is consistent with previous studies[60].

Magnetic free energy analysis

In this section, we present the formula for evaluating the magnetic free energy, which can be linearly decomposed into various physical components. Here, we express the total energy as the sum of the long-range demagnetization energy E_{demag}, short-range exchange energy E_{exch} and entropy term TS as follows:

$$F_{total} = E_{demag} + E_{exch} - TS \tag{2}$$

E_{demag} is considered a long-range term because the demagnetizing field of a magnetic dipole extends over large distances, whereas E_{exch} is a short-range term arising from interactions only between neighboring spins. By observing the contributing factors for each component, we can quantitatively analyse the magnetization reversal mechanism.

Pseudo-exchange energy analysis
The pseudo-exchange energy was evaluated from the magnetic domain image based on the Ising model. The pseudo-exchange energy was calculated via Eq. (3), which considers pixel–pixel interactions for neighbouring pixels from a coarse-grained perspective. In this study, we assume that the magnetization of the sample is oriented vertically, so each image pixel (with magnetization up or down) can be treated as the smallest unit.

$$E_{exch} = \infty - \frac{L}{a} \cdot A_{stiff} \sum_{i}^{n} \sum_{j}^{n} \sum m_{ij} \cdot m_{neighbor} \tag{3}$$

where L represents the sample film thickness (475 μm) and *a* denotes the pixel width (1.66 μm). A_{stiff} is the exchange stiffness constant, for which a value of 5.78×10^{-7} (erg/m) is used for RIG. m_{ij} is the magnetization of the pixel of interest, and $m_{neighbor}$ is the magnetization of its neighbouring pixel. Equation (3) can be used to analyse the energy arising from the domain wall between pixels. A correction factor based on the computational unit size within the sample (L/a) is applied as a proportional coefficient. The size correction for the exchange energy can be adjusted to align with the scale of the magnetic domain structure observations[18]. In this analysis, the exchange interactions among eight neighbouring pixels are evaluated, considering both the first and second nearest neighbours. For the second-nearest pixels, a distance correction factor of $1/\sqrt{2}$ was applied. Notably, in this analysis, the energy is considered from a coarse-grained perspective, given the limitations regarding the scale and binarization of the data. Thus, the calculated pseudo-exchange energy essentially represents the domain wall energy in the observed domain structure.

Pseudo-demagnetization energy analysis
Similarly, the pseudo-demagnetization energy was evaluated on the basis of the magnetic domain image. Since the demagnetization energy originates from the demagnetizing field caused by magnetic dipoles, this analysis was conducted using the perpendicular component of the magnetic moments. The demagnetizing field $h_z^d(r)$ is inversely proportional to the cube of the radius (Eq. (4)).

$$h_z^d(r) = -\frac{1}{2\pi} \sum {}_i \sum {}_j \frac{m_{ij}}{|r|^3} \tag{4}$$

The dipole–dipole interactions were calculated for each pixel, and by summing these interactions across the entire magnetic domain image, the pseudo-demagnetization energy was obtained (Eq. (5)).

$$E_{demag} = \sum_{\boldsymbol{i}} \sum_{\boldsymbol{j}} \sum_{\boldsymbol{r}} h_z^d(r) \cdot m_{ij}(r) \tag{5}$$

To address the long-range nature of the demagnetizing interaction, we here adopted a cutoff radius of $r = 80$, for which the energy is converged to within 1%. This approximation is used throughout to evaluate the peudo-demagnetizing energy while controlling computational cost. This truncated evaluation yields a good approximation of the long-range demagnetizing energy associated with the domain configuration.

Magnetic entropy analysis
Next, to incorporate the contribution of the thermal effect, we evaluated the magnetic entropy of the domain structure. Single-crystalline RIG exhibits a uniaxial magnetic anisotropy perpendicular to the film plane. Given that the surface magnetic pole distribution consists solely of N and S poles, the magnetic domain structure can be approximated by the Ising model. Since the magnetization can only be up or down, the multiplicity *W* can be approximated as a binomial distribution (Eq. (6)).

$$W = {}_n C_k \left(\frac{1}{2}\right)^{\mathrm{k}} \left(\frac{1}{2}\right)^{\{\mathrm{n-k}\}} \tag{6}$$

Here, *n* is the total number of pixels, *k* represents the number of pixels in the up-magnetization state and $n-k$ represents the number of pixels in the down-magnetization state. ${}_n C_k$ is the binomial coefficient, which gives the number of distinct ways to choose *k* up-spin pixels out of *n*. Although the influence of domain walls must be strictly considered, because the volume of the domain walls relative to the sample volume is sufficiently small and the positions of the domain walls in the maze-like magnetic domain structure randomly change, the binomial distribution approximation remains valid. In other words, domain walls occupy a negligible fraction of the material and their random arrangement means they do not significantly alter the overall count of up vs. down domains, so treating the configuration as a random mixture (binomial) is justified. Furthermore, since the binomial distribution applies to discrete random variables and the pixel size is sufficiently small compared with the observation area, the random variable can be reapproximated as a continuous quantity. In this case, the central limit theorem can be applied, and the distribution of the net magnetization (the state variable of the system) can be approximated by a Gaussian distribution.

$$W = A\exp\left(-\frac{(x-\mu)^2}{2\sigma^2}\right) \tag{7}$$

where A is a constant, μ is the mean, and σ is the standard deviation. The variable x in the Gaussian distribution corresponds to the overall magnetization m of the image. In this study, with $x = \{-1,1\}$ and the average magnetic moment $\mu = 0$, the magnetic entropy can be obtained in the form of a simple quadratic function.

$$\ln W = lnA - \frac{m^2}{2\sigma^2} \tag{8}$$

The constants A and σ were obtained via fitting with other energy terms in this study. Since entropy is a dimensionless quantity, it was converted to the dimensions of energy by multiplying it by the Boltzmann constant (k_B = 8.316 × 10^{-16} [erg/K/pixel]), temperature, and an appropriate coefficient to simplify the equation. After this scaling, the entropy contribution can be written in the form shown in Eq. (9), which is proportional to $k_B\left(1-m^2\right)$.

$$S = k_B \ln W \propto \ k_B\left(1-m^2\right) \tag{9}$$

We here note the thermodynamic distinction and physical scale of entropy term. It is important to address the thermodynamic nature of the extended free energy. While standard GL theory implicitly includes microscopic entropic contributions (e.g., atomic thermal fluctuations) in its coefficients, our approach focuses on the mesoscale magnetic domain structure. To capture the complex topology of the maze patterns, we employ a specific morphological treatment that calculates exchange interactions up to the second nearest neighbors, incorporating geometrical constraints beyond simple nearest-neighbor models. Consequently, the -*TS* term introduced here is intended to describe the entropic contribution associated with the mesoscopic domain configuration, which is distinguishable from the microscopic entropy. Empirically, the distinct profiles of the internal energy and entropy terms in Fig. 3 suggest that they represent competing physical factors—energetic stability versus morphological complexity—supporting the validity of this phenomenological extension. Detailed quantitative analysis of this configurational entropy using Shannon entropy is currently underway and will be reported in a future study.

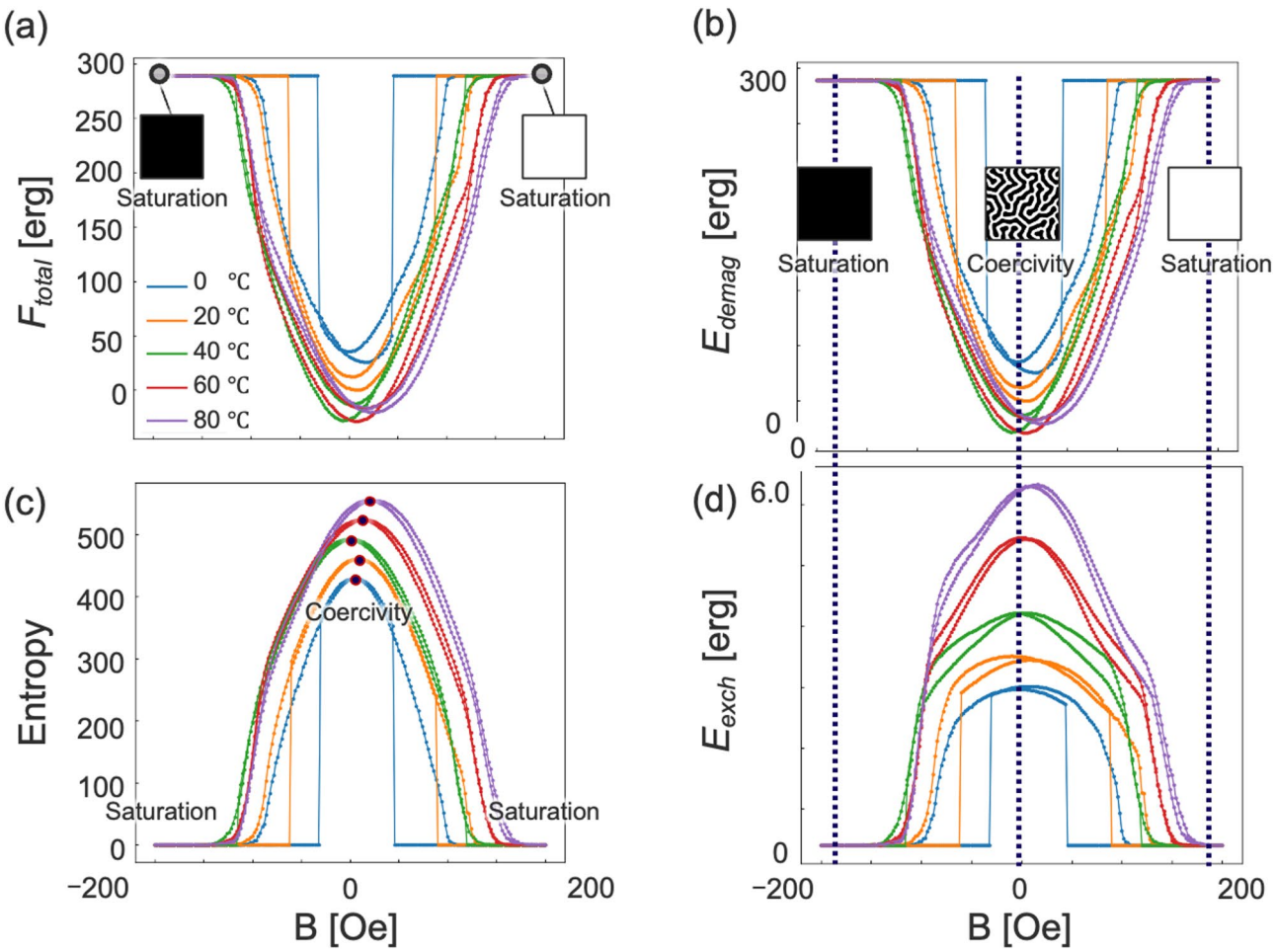

Fig. 3. Energy decomposition in RIG maze domain reversal with total energy (**a**), pseudo-demagnetization energy (**b**), entropy (**c**), and pseudo-exchange energy (**d**). Total and demagnetization energies exhibit concave-down profiles with minima at coercivity, whereas exchange and entropy show concave-up profiles with maxima at coercivity; near coercivity, domain walls become more jagged and longer, consistent with the increase of the exchange (domain-wall) term.

In summary, by modeling the domain configuration as an Ising-like two-state system, we derived an effective entropy term that increases with domain disorder.

The total energy, entropy, pseudo-demagnetization energy, and pseudo-exchange energy were evaluated via the above procedures using domain images of the RIG sample acquired over a full hysteresis loop (external field sweeping from −200 Oe to +200 Oe) at temperatures from 0 to 80 °C (Fig. 3). The total energy has a concave-down shape, with a minimum value in the coercivity region. Similarly, the demagnetization energy has a concave-down shape, with a minimum in the coercivity region. In contrast, the exchange energy shows a concave-up shape, with a maximum in the coercivity region. In this region, the magnetic domain structures become zigzagged, leading to an increase in the domain wall length, which corresponds well with the increase in the domain wall energy captured by the exchange energy term. The entropy also exhibits a concave-up shape, with a maximum in the coercivity region. Note that the slight asymmetry in the hysteresis loops is primarily due to technical constraints, such as the minor offset between the global magnetic field defined by the coil current and the local field in the micro-observation area, as well as slight sample drifts during temperature changes. Through this analysis, the classical energy landscape was confirmed to be in accordance with that observed in the literature. These results indicate that the developed model can be used to model magnetic domains at various temperatures and magnetic fields.

Modelling of the extended Landau free energy

We constructed the extended Landau free energy landscape based on the structural features of the magnetic domains and the free energy (Fig. 4). This landscape, with the total energy labelled accordingly, was obtained by reducing the microstructure of the magnetic domains to a low-dimensional space via principal component analysis (PCA)[62]. PCA is a highly interpretable machine learning method suitable for deepening interpretations via eigenvectors[62]. Since the Euclidean distance is preserved in the latent PCA space, a relationship between the change in the magnetic domains and the corresponding change in total energy can be established. When the displacement of data points is small, the magnetic domain structure remains relatively unchanged; when it is large, a considerable change in the structure occurs. Each data point is associated with the total energy, allowing structural analysis of the magnetic domains associated with the energy cost. Additionally, each point in the scatter plot corresponds to a magnetic domain image. The data points trace a continuous trajectory in PCA space—rather than forming disconnected clusters—indicating a gradual, field-driven evolution of domain morphology. The resulting PCA plot is fully consistent with earlier studies of field-dependent maze domains[60]. Along the magnetization reversal path in Fig. 4, the microstructure evolves continuously—from saturation (all spins aligned), through elongation (narrow stripes stretched) and widening (reversed domains broaden), approaching coercivity (net magnetization ≈ 0), widening, and finally reaching annihilation (remnant minority domains disappear).

In the extended Landau free energy landscape, significant changes in energy are observed from saturation through the nucleation and elongation processes, whereas from widening to the coercivity point, the energy change is minimal, resulting in a flat landscape (Fig. 4). These results indicate that a small energy cost is required to change the magnetic domains near the coercivity point, which aligns well with the typical behaviour of soft magnetic materials.

PCA was employed to reduce the dimensions of the structural changes extracted from the PDs. PC1 and PC2 represent the principal component vectors obtained from PCA. In this analysis, PC1 serves as the feature that best represents the structural changes, accounting for the largest variance in the domain morphology. The physical meaning of these components is determined through correlation analysis with physical parameters (details provided in the Supplemental Fig. 2). While PC1 showed a clear correlation with the magnetization state such as exchange, demagnetization, total energy and entropy, PC2 and higher-order components did not exhibit clear physical correlations. Thus, PC1 effectively describes the energy landscape. This model enables the microstructure to be connected with macroscopic functions within the data space. Because energy values are not used as PCA inputs, any large variance or apparent outlier in the feature space corresponds to a physically distinct domain state, providing additional insight. Focusing on the coercivity point at various temperatures, PC1 clearly linearly increases with temperature, whereas PC2 remains nearly zero with increasing temperature. This result suggests that PC1 is a useful feature for describing the coercivity and temperature dependence. By analysing the energy gradient and performing component analysis with respect to PC1, we aim to causally analyse the magnetization reversal mechanism. In the following section, we focus on PC1 to conduct correlation analysis with various physical properties and energies to improve our understanding of the physical interpretation of the results.

Correlation analysis between features and physical quantities

To further analyse the magnetization reversal mechanism, we examined the correlation between PC1 and energy to provide a physical interpretation of the features. For clarity, we restrict the discussion to the demagnetization branch—from positive saturation to the coercivity region—because this segment captures the full sequence of domain nucleation, growth, and annihilation in a single, monotonic field sweep. The total energy monotonically decreases from the saturation region to the coercivity region during magnetization reversal, with a noticeable kink (Fig. 5a). Near the coercivity region, the energy landscape is flat, and this flat region expands with increasing temperature. This result suggests that thermal fluctuations facilitate changes in magnetic domains.

Next, we analysed the correlation between PC1 and the order parameter, i.e., magnetization M (Fig. 5b). The results show that PC1 can be expressed as a quadratic function of M, leading to the following regression equation:

$$PC1 = -1.12M^2 + 3.74M + 125.98 \tag{10}$$

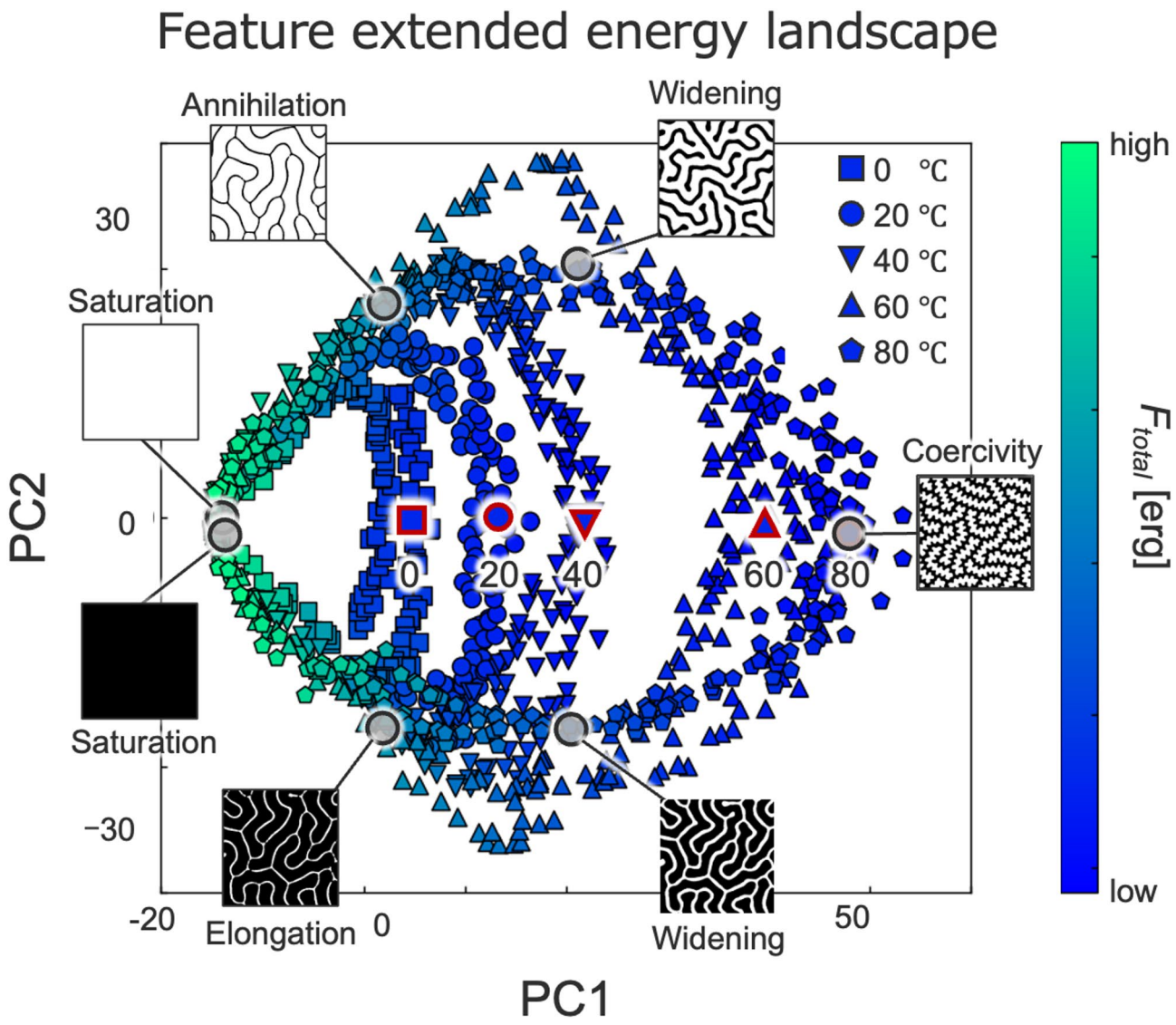

Fig. 4. Extended Landau free energy landscape. Using the structural features analysed via the PH and the free energy, a new energy landscape was constructed in data space. The displacement of data points corresponds to changes in the images, which can also be associated with changes in energy. This allows structural analysis associated with the energy consumed (or accumulated) during each process, enabling connection of the microscopic structures to macroscopic functions across hierarchies. The region near the coercivity point exhibits a flat energy landscape, indicating that small energy cost is required to change the magnetic domains. It is consistent with the typical behaviour of soft magnetic materials. Focusing on the coercivity point at various temperatures, PC1 clearly linearly increases with temperature, whereas PC2 remains nearly zero with increasing temperature, indicating that PC1 is a useful feature representing the coercivity and temperature.

This analysis establishes the relationship between M and PC1. In conventional Landau theory, M serves as the order parameter for magnetization; however, in this model, M is replaced by a structural feature, effectively bidirectionally connecting the physical space with the data space. Additionally, the polynomial function simplifies differentiation, which is advantageous for analysis of the energy gradient and energy consumption, as discussed in the next section. Notably, this quadratic dependence was consistently observed across the other temperatures examined. Further correlation analyses involving PC2 and higher order principal components are described in the Additional Information.

All the energy landscapes are flat near the coercivity region, indicating that the magnetic domain structure easily changes near the coercivity region.

Next, we decomposed the free energy into three components: the pseudo-demagnetization energy, pseudo-exchange energy, and entropy. The pseudo-demagnetization energy steadily decreases with PC1, with its slope varying with temperature (Fig. 5c), similar to the behaviour of the total energy with PC1. In contrast, the pseudo-exchange energy steadily increases with PC1 (Fig. 5d). Near the coercivity region, the energy landscape flattens, and as the temperature increases, this flat region shifts to the right and expands. Notably,

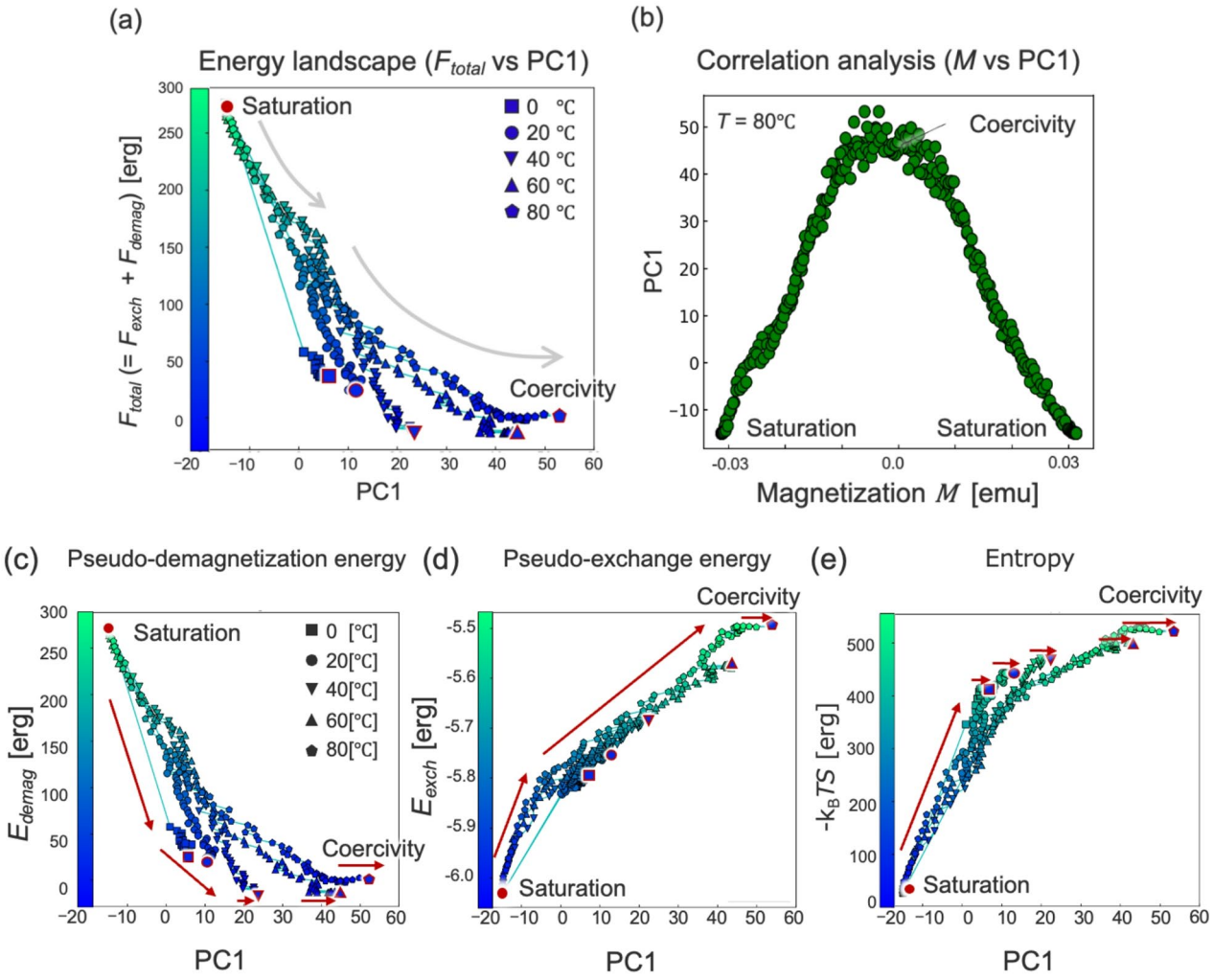

Fig. 5. Correlation analysis of physical properties and features. (**a**) Total energy and PC1: monotonic decrease with a kink in the middle. (**b**) PC1 vs. magnetic moment approximated by a quadratic curve. (**c**) Pseudo-demagnetization energy and PC1: monotonic decrease with a kink in the middle. The behaviour is similar to that of the total energy. (**d**) Pseudo-exchange energy and PC1: monotonic increase with a kink in the middle. The behaviour is inverse to that of the pseudo-demagnetization energy, with values two orders of magnitude smaller. (**e**) Entropy and PC1: monotonic decrease with a kink in the middle, similar to that of the pseudo-exchange energy.

the pseudo-exchange energy is much smaller, by two orders of magnitude, than the demagnetization energy. The entropy also steadily increases with PC1, with a kink in its landscape that flattens near the coercivity region (Fig. 5e), mirroring the trend in the exchange energy with PC1. This concordance could indicate a coupling between domain-wall geometry and entropy: because the exchange term scales with wall length, the matched PC1 dependence implies that wall proliferation and increased zig-zag roughness track the rise in structural complexity. All the energy landscapes flatten near the coercivity region, suggesting that changes in the magnetic domain structure occur more easily in this region. Our model shows that all the energy components have a low cost for altering the magnetic domain structure near the coercivity region, which aligns with the typical behaviour of soft magnets[2,16,47–50,60].

Classically, the demagnetization energy is expressed as the square of the magnetization M (Eq. (5)). Similarly, the exchange energy, which results from the inner product of the magnetization, is expressed as the square of M (Eq. (3)). The entropy, which is approximated by a binomial distribution, is similarly represented as the square of M (Eq. (9)). Thus, each energy term can be expressed as the square of M (Fig. 3). In the data space, PC1 is also represented as the square of M, as shown in Eq. (10). Thus, the energy terms having the same dimension is reasonable, as is all the energy terms exhibiting a linear relationship with PC1. From this perspective, the next step is to focus on the nonlinear behaviour in the energy landscape within the data space and perform gradient analysis to detect outliers. These findings demonstrate that PC1 simultaneously encodes morphological evolution and physically meaningful energy terms, providing a robust platform for subsequent causal inference in magnetization-reversal process.

Discussion

In this study, we aimed to unravel the magnetization reversal mechanism by performing a causal analysis of the energy landscape using eX-GL. This analysis allowed us to visualize the key energy barriers in the reversal process and to identify how different energy contributions – notably the entropic term – causally influence the progression of reversal. These findings directly address our original objectives and provide deep insights into how the energy landscape governs magnetization reversal process. We performed a detailed causal analysis of magnetization reversal mechanisms by examining the energy landscape gradient and their individual components. By analyzing these gradients, we heuristically identified the four energy barriers with the largest deviations as 'outliers,' which are discussed in detail in next section and Fig. 6. Decomposing the free energy into its components allowed us to quantitatively determine which physical components contributed to each barrier. This approach enabled us to quantitatively analyse the interrelationships between individual components of the free energy (such as exchange interactions and the entropic term), thereby deepening our understanding of the magnetization reversal mechanism.

In the eX-GL model, the system's energy gradient is analysed in the data space. By modifying Eq. (1) to incorporate the feature PC1, we derived Eq. (11).

$$H_{eff} = -\frac{\partial F}{\partial M} = -\frac{\partial F}{\partial PC1}\frac{\partial PC1}{\partial M} \tag{11}$$

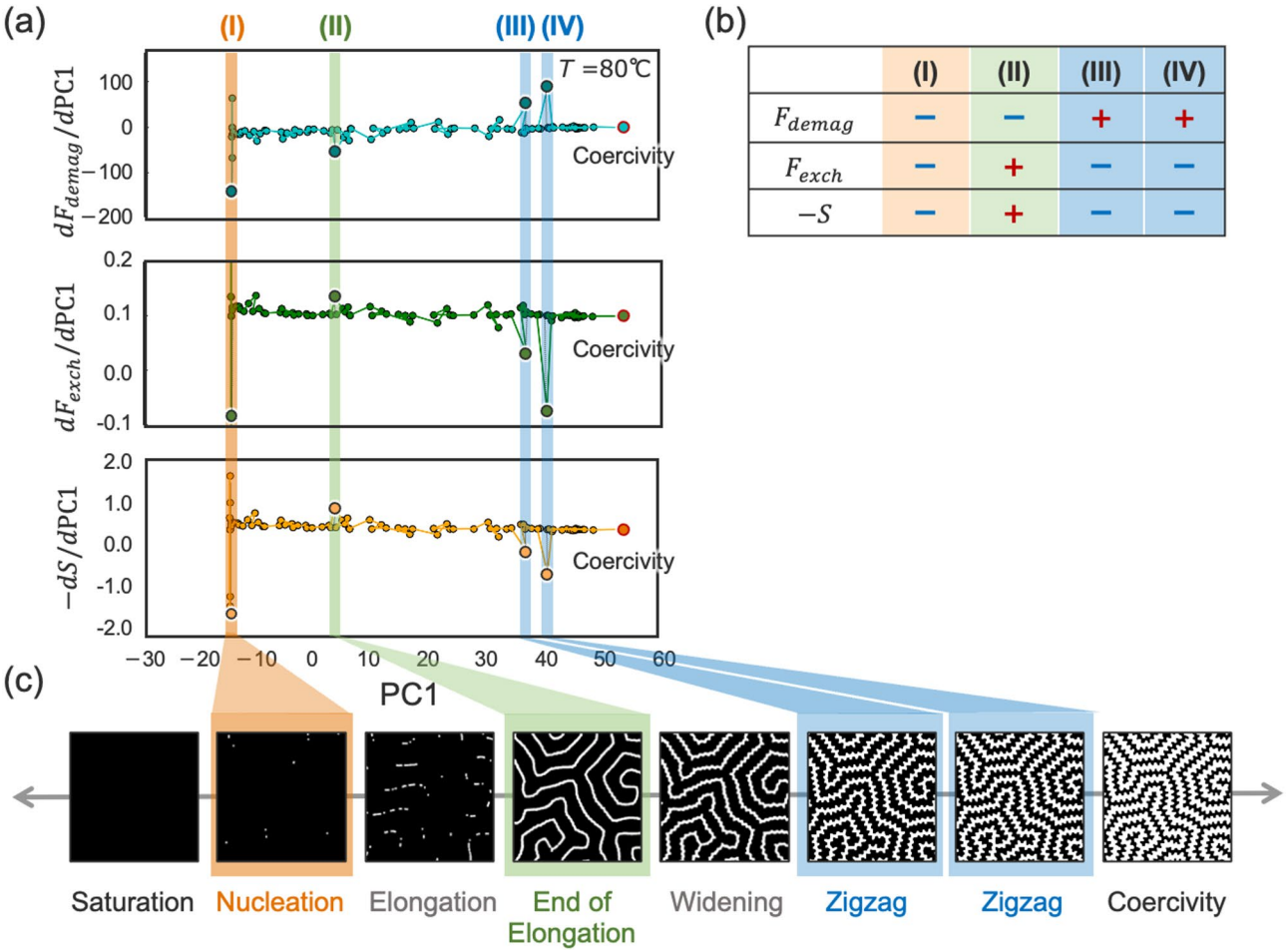

Fig. 6. (**a**) Energy barriers in the data space associated with individual physical effects (demagnetization, exchange, and entropy), identified via gradient and component analysis. Four prominent barriers (I–IV) appear as outliers at corresponding positions in each energy component. (**b**) Sign of energy transfer associated with the magnetic domains. (**c**) Magnetic domain structures with different PC1 values. (**a**–**c**) provide a deeper understanding of the magnetization reversal mechanism. At barrier (I), all energy components are negative, indicating that substantial energy is required to break the ferromagnetic order and nucleate reversal domains. Barrier (II) corresponds to the formation of the maze magnetic domain structure. This barrier marks a transition from the elongation mode to the widening mode in domain propagation (**c**). This mode transition requires exchange energy and entropy costs. Barriers (III) and (IV) show a reversal in sign, where demagnetization energy is consumed and transferred to the exchange energy and entropy. This result indicates that energy is spent in complicating the zigzag structure of the magnetic walls, thereby stabilizing the system (**c**). The demagnetization energy, exchange energy, and entropy are closely coupled with each other.

The first term on the right-hand side represents the local gradient of the free energy landscape with respect to the feature, whereas the second term corresponds to the transformation operator between the feature and the physical magnetization. This formulation maintains mathematical consistency with conventional GL theory. In this extended model, the conventional order parameter M is replaced by the principal component feature PC1 as the explanatory variable, representing the structural state of the magnetic domain. Since the second term is well-approximated by a simple linear function (from Eq. (10)), our analysis focuses on the first term to investigate the magnetization reversal process. Using Eq. (2) along with Eq. (11), we performed gradient analyses for each energy component of the system. The significant steep energy barrier was extracted as an outlier.

Figure 6 shows the energy barriers in the data space associated with individual physical effects detected via gradient and component analysis. The energy barriers are illustrated by decomposing the total energy into the demagnetization energy (dipole–dipole interactions), domain wall energy (exchange interactions), and entropy. The horizontal axis represents PC1 and corresponds to the obtained principal component scores (Fig. 4). For simplicity, the data for the demagnetization process from saturation to the coercivity region are displayed. The energy gradients of each component are nearly constant owing to the monotonic change in the energy landscape. Additionally, sharp outliers in the energies and entropy can be observed at specific points (I-IV), resulting in an increasingly complex magnetic domain structure as the magnetization reversal process progresses. Notably, we identified as outliers the four energy barriers with the largest deviations from the baseline. These outliers suggest that abrupt energy changes occur, either inhibiting or promoting the magnetization reversal process. To gain deeper insight into the magnetization reversal process, we next investigate the sign and contribution of each energy component at each barrier.

At barrier (I), which corresponds to nucleation of the magnetic reversal domains, all the energy components are negative. A negative value here indicates that energy is absorbed from the external field by the system, facilitating the creation of reversed domains. This result suggests that energy is transferred from the external field and used to generate reversal domains, thereby promoting magnetization reversal. The fact that the demagnetization energy, exchange energy, and entropy all have the same sign implies that considerable energy is required to break the ferromagnetic order in the initial stages of magnetization reversal. Because all three components require energy input (none is releasing energy), this strongly supports the idea that a substantial energy barrier must be overcome to disrupt the initial ferromagnetic alignment. This finding aligns well with the general understanding of reversal domain nucleation[9,14,16,47], as nucleating a reversed domain typically necessitates overcoming a significant energy barrier to disturb the initial magnetic order. The fact that these results were obtained in a data-driven manner without preconceived biases is particularly valuable.

Next, we focus on energy barrier (II). As this barrier is approached, the reversal domains elongate and then form characteristic maze-like magnetic domains. Beyond this point, the domain structure gradually widens and shifts to a zigzag pattern. This result suggests that barrier (II) marks the transition from elongation to widening in domain propagation, with a change in the domain growth mode. At this stage, the demagnetization energy is negative, whereas the exchange energy and entropy are positive, indicating an interplay among these energies: the reduction in demagnetization energy is accompanied by an investment of exchange energy and an increase in entropy. Overcoming this energy barrier signifies a shift in the domain growth mode, which requires the acquisition of demagnetization energy, the consumption of exchange energy, and an increase in entropy. Such energy trade-offs are consistent with known magnetization reversal behavior, where demagnetization energy is reduced at the expense of creating additional domain walls and disorder in the domains. Although this structural change can be visually observed in magnetic domain images, the fact that the mechanism was automatically analysed is remarkable, especially since the automated results agree with established interpretations of the domain evolution.

At barriers (III) and (IV), the signs are reversed compared with the sign at barrier (II). A decrease in the demagnetization energy and increases in both the exchange energy and entropy are observed. The exchange energy and entropy both have positive signs and are correlated, whereas the demagnetization energy has a negative sign. The results confirm that demagnetization, exchange, and entropy are coupled. The domain wall energy and the entropy sharing the same sign is responsible for the increase in the domain wall length and the resulting complexity of the maze magnetic domains. In other words, when both the domain wall energy and entropy increase, total wall length grows and the domain pattern becomes more mazed. The system stabilizes itself by lowering the total free energy: it reduces demagnetization energy by subdividing the domain structure, while accepting the costs associated with domain walls and configurational entropy. The observed decrease in demagnetization energy alongside increases in exchange energy and entropy, together with the growth of wall length and maze complexity, is consistent with this mechanism. While it is well known that reducing demagnetization by subdividing domains increases wall (exchange) energy, our analysis shows that part of this cost is also borne by entropy. In other words, exchange interactions and entropy are always coupled, and an increase in the domain wall length results in a more complex magnetic domain structure, which provides a reasonable explanation for the observed behaviour. The ability to elucidate the magnetization reversal mechanism through quantitative analysis of the energy transfer between various physical components is important. This component-wise energy analysis quantitatively solidifies the mechanism of complex magnetization reversal.

Next, we visualized the factors contributing to entropy. We focused on barriers (III) and (IV), because these two barriers correspond to significant entropy-driven jump. Accordingly, we conducted a detailed analysis of microstructural changes with the energy barriers, particularly those related to entropy. We aimed to quantify the complexity of the magnetic domains, which is challenging to analyse visually, visualize the spatial distribution of the entropy and extract hidden information. By visualizing the spatial distribution of the entropy, the mechanism underlying the complexity of the maze magnetic domains can be determined. Here, we employ the elementwise product to construct a feature vector that describes both the entropy barrier and the domain structure[47,60], following a similar approach used in previous studies[47–60]. In the energy gradient analysis described by Eq. (12),

we utilize $\Delta PC1$, which is the difference in PC1 scores. $\Delta PC1$ is the inner product of ΔPD (the difference in the PDs) and u_1 (the principal component vector of the PDs).

$$\Delta PC1 = \Delta \boldsymbol{PD} \cdot \boldsymbol{u}_1 \tag{12}$$

We can write $\Delta PC1$ as a vector via the following Eq.

$$\Delta \boldsymbol{PC1} = \Delta \boldsymbol{PD} \odot \boldsymbol{u}_1 \tag{13}$$

Here, $\odot$ represents the elementwise product, which creates a vector by taking the product of each corresponding element in two vectors. Each element in this vector is created by multiplying the differences in the PDs ($\Delta \boldsymbol{PD}$) with the basis vector $\boldsymbol{u}_1$. By adding all the elements of $\Delta \boldsymbol{PD}$, the scalar $\Delta PC1$ can be obtained, which aligns with the PCA results given by Eq. (12) and the energy landscape in Fig. 4. Essentially, the elementwise product of $\Delta \boldsymbol{PD}$ and $\boldsymbol{u}_1$ allows $\Delta PC1$ to be reconstructed as a vector. This vector is generated for each energy barrier and has the same dimension as the PD, allowing us to analyse the microstructure around specific energy barriers. This method has been validated in previous research[47–60].

Using the elementwise product, the PDs for entropy barriers (III) and (IV) can be reconstructed, as shown in Fig. 7a and c. This reconstruction highlights the persistence features that change at each entropy barrier, pinpointing where entropy-driven transformations occur in the domain structure. At entropy barrier (III), generators are plotted along the central region of the magnetic domains (Fig. 7b). This result captures the increase in the complexity of the zigzag pattern of the domain structure, demonstrating reasonable and consistent results. While the increased complexity at barrier (III) is qualitatively observable in the domain images, the automatic identification ability is highly beneficial for functional analysis, providing an objective means to pinpoint such changes and representing a significant improvement over reliance on visual observation alone. At entropy barrier (IV), the spatial distribution of generators is sparse (Fig. 7d). With some exceptions, the generators are plotted in the regions where the magnetic domains curve. This result suggests that these are regions where the entropy increases. Given that PH analyses are sensitive to medium-range order components, these findings may capture medium-range interactions driven by the demagnetization energy. Such subtle microstructural changes are difficult to visually detect, and our approach appears to effectively visualize hidden information involving entropy interactions with the demagnetization effect. The results suggest that the magnetic domain structure changes at barriers (III) and (IV) represent different growth modes in terms of shape and physical effects. Barrier (III) (Fig. 7b) is more sensitive in capturing the zigzag structure of domain walls than barrier (IV) (Fig. 7d), indicating that the increase in complexity due to entropy has a stronger influence on the exchange effect than on the demagnetization effect. Accordingly, the PD is a useful descriptor that accounts for both morphology and energy. This approach enables the successful extraction and analysis of the complex nature of magnetic domains, which has been difficult to visually detect, thereby improving our understanding of the underlying mechanism. Thus, our advanced material analysis method captures hidden information.

The eX-GL model enables the microstructure to be successfully connected to the macroscopic functions in the magnetization reversal process across material hierarchies. It also enables causal analysis of the mechanisms and visualization of hidden information. Since free energy is a universal thermodynamic concept, various energy terms can be substituted and analysed, with potential application to a wide range of material challenges. Since the present formulation employs the Ising approximation, its direct application is limited to materials with strong uniaxial anisotropy, where the magnetization is predominantly perpendicular to the film plane (e.g., RIG). However, the eX-GL framework itself is highly versatile and applies to non-Ising systems by adapting the energy functional to continuous vector fields (e.g., XY or Heisenberg models). We have already demonstrated the validity of this framework for soft magnetic materials, including the loss analysis in Non-Oriented Electrical Steel assuming an XY-like model[63] and the defect pinning analysis in Permalloy[47,48]. Regarding hard magnetic materials, the theoretical foundation has been established[19,53]. By utilizing the concept of the effective field derived from the extended free energy, this framework can universally describe the coercivity mechanism regardless of the material's hardness. Furthermore, we are actively extending this framework to more complex vector textures. We are sequentially deploying this approach to develop a general-purpose model capable of analyzing mesoscale magnetic domain structures in broader systems, including Skyrmions. Furthermore, by analysing the Gibbs free energy or elastic energy, the model could be applied to crystal growth and mechanical properties[64]. Moreover, the maze magnetic domain structure has long been the subject of fractal analysis, suggesting that this approach could contribute to fundamental areas such as nonequilibrium physics[7,14]. Looking forward, the extended Landau free energy model is expected to find broad applications, ranging from fundamental research to applied materials science.

Conclusion

In this study, to comprehensively analyze the complex magnetization reversal mechanism interacting with the maze magnetic domain structure and the thermal effect, we extended the Landau free energy model by incorporating entropy. The model was constructed by integrating structural analysis via Persistent Homology, energy analysis, and Principal Component Analysis. By constructing a novel energy landscape in data space, the model enabled robust connection of the microscopic domain structure to macroscopic functions. As a form of explainable artificial intelligence, the model enabled causal analysis of the magnetization reversal mechanism through gradient analysis and component analysis of the energy landscape.

As a result, we could quantitatively analyse the energy transfer among the demagnetization effect, exchange effect, and entropy. Notably, the entropy was found to be consistently coupled with the exchange effect, resulting in an increase in the complexity of the magnetic domains with increasing domain wall length. This coupling

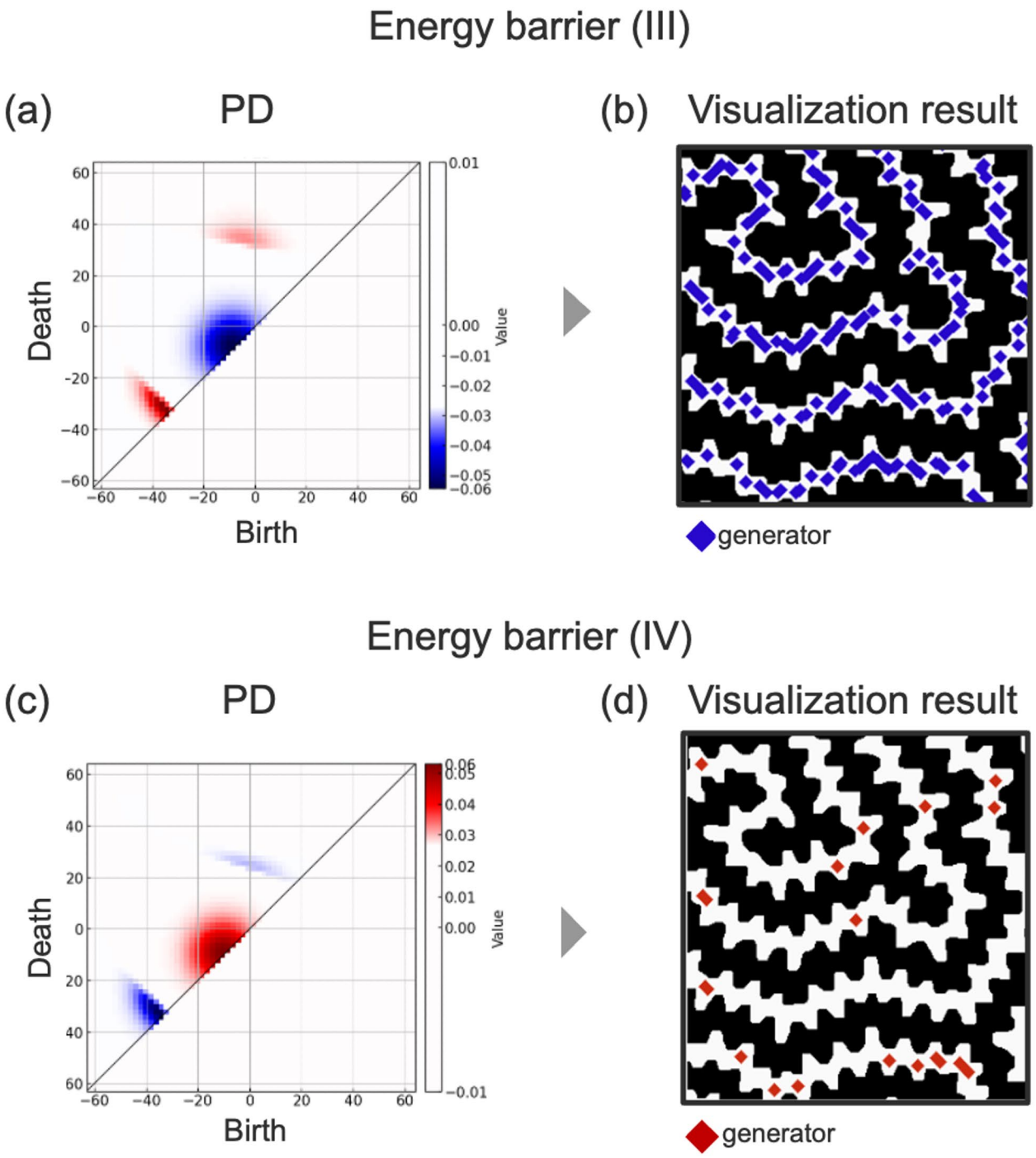

Fig. 7. Visualization of the entropy barriers in magnetic domain images via the elementwise product. In the elementwise product, the inner product used in PCA is replaced with the product of the individual vector elements. The feature vector contains information on both structural changes and entropy changes (**a**, **c**), allowing analysis of microstructural changes with a focus on specific entropy barriers (**b**, **d**). The generators at barrier (III) identify the increasing complexity of the zigzag patterns of the maze magnetic domains, yielding reasonable results. At barrier (IV), the sparse spatial distribution of generators suggests that the method captures the complexity of medium-range order. The findings indicate that hidden information, such as the interaction between the entropy and demagnetization energy, can be effectively visualized.

allowed automated interpretation of the complex magnetization reversal mechanism. Furthermore, by conducting a detailed analysis of energy barriers using the elementwise product, we extracted hidden information. With this approach, the origin of the increase in entropy was linked to the initial magnetic domain structure, providing a clear illustration of the underlying mechanism. Specifically, we could distinguish the roles of the entropy barriers and identify them in the initial image. This approach effectively automates the interpretation of the complex

magnetization reversal process and enables successful extraction of hidden mechanisms that are not easily discernible through conventional visual inspection. Because free energy is a universal thermodynamic metric, our entropy-feature-eXtended Ginzburg-Landau framework can extend from inhomogeneous magnets to any system undergoing phase-like transitions. Real-space decomposition of energy terms supplies actionable design cues—for instance, tailoring defect landscapes in magnetic media to lower switching energy and refine reversal control. Thus, we not only clarify maze-domain reversal mechanics but also deliver a general strategy for probing complex mesoscale energy landscapes. Future work can add further physical variables or target new phenomena, broadening the framework's reach in computational materials science.

Methods

Sample

The sample used for the measurements was a commercially available RIG single-crystalline thin film fabricated via the liquid phase epitaxy (LPE) method. A sample with a film thickness of 475 μm (substrate size: 11 mm × 11 mm) was employed. RIG is known to form clear and complex maze magnetic domains near the coercivity region, making it an ideal sample for acquiring magnetic domain data, examining the contribution of entropy to the magnetic domains, and modelling extended free energy frameworks[7,31,33].

Magnetic domain observation

Kerr microscope system was used to acquire temperature- and magnetic field-dependent magnetic domain structure data. The setup consisted of a metallurgical microscope (Zeiss Axioscope Vario, Germany), a projection electromagnet with a perpendicular configuration (GMW Associates 5203 S/K, USA), and a cooling/heating stage for microscopy (LINCAM 10033 L, UK), allowing automated acquisition of magnetic domain data under arbitrary magnetic fields and temperatures[7,31,33]. Magnetic domain structure measurements were conducted with the polar Kerr configuration to measure the spatial distribution of the perpendicular magnetization. The polarizer was rotated a few degrees from the crossed Nicol configuration to capture magnetic domain images at the angle where the magnetic contrast was maximized. The wavelength coefficient of the 45-degree rotator used during the measurements was 0.065 deg/nm, which provided a sufficient Kerr rotation angle, resulting in clear magnetic contrast.

An external magnetic field was applied perpendicular to the sample surface and was quasistatically varied within the range of 200 Oe to -200 Oe in 2 Oe increments. Approximately 400 magnetic domain images per hysteresis loop were continuously obtained. The measurement temperature was set at 0, 20, 40, 60, and 80 °C to assess the temperature dependence of the magnetization reversal process. The field of view was 1700 × 1700 μm, and the image size was 1024 × 1024 pixels. Each pixel was recorded in 14-bit grayscale, with the exposure time set to 250 milliseconds, fully utilizing the 14-bit dynamic range. The magnetic moment was evaluated using the average magnetic contrast of the magnetic domain structures, and a macroscopic magnetic hysteresis curve was constructed. The saturation magnetization was 3.2×10^3 emu/cc. To eliminate uneven illumination and noise, background processing, median filtering, and morphological transformations were employed. The magnetic domain structures were binarized into black and white images via Otsu's method. The measurements were repeated multiple times to confirm the reproducibility of the magnetization hysteresis loop and the robustness of the extracted features.

Persistent homology

The basic concepts of the persistent homology (PH) analysis and the procedure for extracting information from magnetic domain data are as follows[54–59]. In this study, filtration was applied to binary data. Each pixel in the image had a value of either 1 (white) or 0 (black), corresponding to up or down magnetization, respectively. In the PH analysis, the Manhattan distance from each pixel to the boundary between the white and black pixels was analysed (Fig. 8a). By continuously varying the threshold between the black and white pixels in terms of the Manhattan distance, the boundary was expanded or contracted (Fig. 8b). During this process, the threshold b at which a "hole" was generated (birth) and the threshold d at which it disappeared (death) were recorded to extract the structural features. The pair (b, d) is referred to as a generator, providing information that characterizes the shape of the hole. Processing of the entire image in this manner resulted in a persistence diagram (PD) (Fig. 8c).

Persistent homology analysis was performed for both black PH_0^b and white PH_0^w domains, obtaining 400*2 persistence diagrams per sample (400 images $\times$ 1 loop $\times$ 2 types). These diagrams were converted into Persistence Images (PI) to generate 1D feature vectors. The weighting parameters were set to C = 0 and $p = 0$, and the smoothing parameter was set to $\sigma = 11$. The mesh range was defined as $\{(b, d) \in [-32, -32] \times [32,32]\}$, resulting in a PI with 2048 components for each color domain. By combining the PIs for PH_0^b and PH_0^w, we obtained a feature vector with 4096 components per image. Finally, all feature vectors acquired in this experiment were stacked vertically to create a 2D matrix with dimensions of (4096 $\times$ 2400), representing the magnetization reversal processes for 4 loops across 3 samples. The computational time for the PCA on this matrix was approximately a few minutes.

The PD provides a structural description of the data, enabling quantification of microstructural shape information (Fig. 8d). For example, stripe structures have generators along the diagonal of the PD, as b and d have similar values, whereas bubble structures have generators in the second quadrant. The boundary movement direction can be processed for both positive and negative values—with structure expansion in the positive direction and contraction in the negative direction. With this process, the holes can be described, and the connectivity of the structure can be obtained.

In the analysis of magnetic domain structures during magnetization reversal, extraction of features from both white and black domain structures is beneficial; thus, PH analysis was performed for both types of structures. The distribution of (b, d) pairs appearing on the PD can be used to describe the microstructure, and each generator

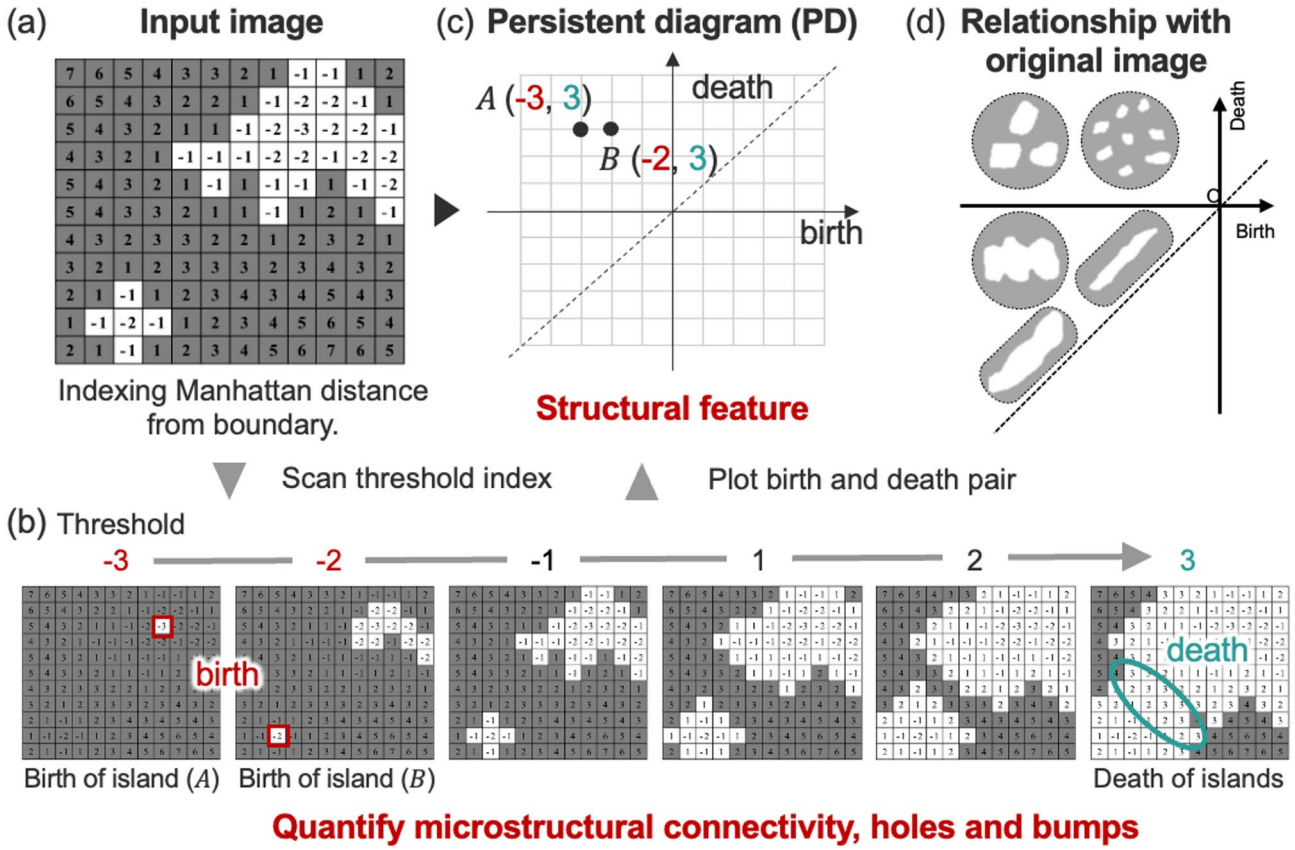

Fig. 8. Schematic sequence of the persistent homology (PH) analysis. For the input binarized image, each pixel is indexed by the Manhattan distance from the boundary (**a**). As the Manhattan distance threshold is scanned, the thresholds at which islands form, connect, and disappear are analysed (**b**), and a persistence diagram (PD) is constructed (**c**). The PD represents the connectivity of the islands and the presence of holes, and its correspondence with the original structures (such as bubbles, stripes, and constricted shapes) is illustrated in a schematic diagram (**d**). The PD serves as a valuable descriptor for explaining the magnetic domain microstructure.

on the PD can be reverse-mapped to its corresponding original spatial coordinates, allowing the generator to be traced to the coordinates in the original magnetic domain structure. By combining PH analysis with machine learning, relationships between microstructures and various physical parameters can be established. Previous studies have reported that the PD contains information about the stability of the system and can be used for energy estimation[47]. It can also be used to estimate physical properties such as magnetization and to classify magnetic domains.

PCA

Principal component analysis (PCA) is a typical unsupervised machine learning technique through which a high-dimensional vector $\{\boldsymbol{x_i} \mid x_1^i, \ldots, x_p^i\}$ is transformed to a lower-dimensional vector $\{\boldsymbol{y_i} \mid \left(y_1^i, \ldots, y_m^i\right),\ m < p\}$[62]. A projection matrix $\boldsymbol{W} = \{\boldsymbol{w}_1, \ldots, \boldsymbol{w}_i \mid \boldsymbol{w}_i = (w_1, \ldots, w_p)\}$is created to project the data into a lower-dimensional space while preserving as much of the variance information from the high-dimensional space as possible (Eq. (14)). Here, let $\boldsymbol{x} = \{\boldsymbol{x}_1, \ldots, \boldsymbol{x_n}\}$, and $\boldsymbol{y} = \{\boldsymbol{y}_1, \ldots, \boldsymbol{y_n}\}$.

$$y = Wx \tag{14}$$

The vectors $\boldsymbol{w}_i$ that constitute the projection matrix are the basis vectors (PCA loadings), and the projected vectors are the principal components $\boldsymbol{y_i} = (y_1^i, \ldots, y_m^i)$. The principal components are sequentially labelled PC1, PC2, …, PCm, with smaller numbers indicating greater explanatory power. The advantages of PCA include both its ability to visualize distances and trends among data in a low-dimensional space and its capacity to extract intrinsic features within the data as basis vectors. Since these basis vectors are orthogonal, the Euclidean distances between data points are preserved, allowing calculation of the correlations between the distance and physical parameters without distorting the space.

When applied to a magnetic domain structure, PCA is expected to quantify the complexity and connectivity of the microstructure, enabling visualization of complex changes in the magnetic domain. Specifically, the PD was converted into a vector according to a positive definite kernel, and a large matrix was created by stacking

a series of data from the magnetization reversal process. PCA was then employed to reduce the dimensionality to two principal components. This approach allowed the change in the PD to be represented with a few basis vectors, facilitating visualization of the magnetization reversal process in a low-dimensional space. By analysing the internal energy at each point, a new energy landscape in the information space could be constructed.

Data availability

The datasets analysed in the current study are available in the Zenodo repository, [https://doi.org/10.5281/zenodo.17562771](https:/doi.org/10.5281/zenodo.17562771).

Code availability

The custom source code used for high-speed energy analysis in this study is proprietary due to planned commercialization and is not publicly available. The core algorithm and calculation methods, which are sufficient for methodological validation and replication, are described in detail in this paper.

Received: 4 December 2025; Accepted: 6 February 2026
Published online: 11 February 2026

References

1. Pei, R., Zeng, L., Chen, X. & Liu, X. Studies of high-efficiency electrical steels used in electric vehicle motors. *J. Shanghai Jiaotong Univ. Sci.* **17**, 319–322 (2012).
2. Silveyra, J. M., Ferrara, E., Huber, D. L. & Monson, T. C. Soft magnetic materials for a sustainable and electrified world. *Science ()* 362, (2018).) 362, (2018). (1979).
3. Akagi, H. et al. Power-Loss breakdown of a 750-V 100-kW 20-kHz bidirectional isolated DC–DC converter using SiC-MOSFET/SBD dual modules. *IEEE Trans. Ind. Appl.* **51**, 420–428 (2015).
4. Hayward, T. J. & Omari, K. A. Beyond the quasi-particle: stochastic domain wall dynamics in soft ferromagnetic nanowires. *J. Phys. D Appl. Phys.* **50**, 084006 (2017).
5. Li, J., Sepehri-Amin, H., Sasaki, T., Ohkubo, T. & Hono, K. Most frequently asked questions about the coercivity of Nd-Fe-B permanent magnets. *Sci. Technol. Adv. Mater.* **22**, 386–403 (2021).
6. Kronmüller, H., Durst, K. D. & Sagawa, M. Analysis of the magnetic hardening mechanism in RE-FeB permanent magnets. *J. Magn. Magn. Mater.* **74**, 291–302 (1988).
7. Han, B. S., Li, D., Zheng, D. J. & Zhou, Y. Fractal study of magnetic domain patterns. *Phys. Rev. B.* **66**, 014433 (2002).
8. Toga, Y., Miyashita, S., Sakuma, A. & Miyake, T. Role of atomic-scale thermal fluctuations in the coercivity. *NPJ Comput. Mater.* **6**, 67 (2020).
9. Kittel, C. & Galt, J. K. Ferromagnetic domain theory. in 437–564 (1956). https://doi.org/10.1016/S0081-1947(08)60136-8
10. Chikazumi, S. Mechanism of high coercivity in rare-earth permanent magnets. *J. Magn. Magn. Mater.* **54–57**, 1551–1555 (1986).
11. Bathany, C., Le Romancer, M., Armstrong, J. N. & Chopra, H. D. Morphogenesis of maze-like magnetic domains. *Phys. Rev. B.* **82**, 184411 (2010).
12. Kronseder, M. et al. Real-time observation of domain fluctuations in a two-dimensional magnetic model system. *Nat. Commun.* **6**, 6832 (2015).
13. Iwano, K., Mitsumata, C. & Ono, K. Maze energetics revealed by a large-scale two-dimensional Ginzburg-Landau type simulation. *J Appl. Phys* **115**, (2014).
14. Seul, M. & Andelman, D. Domain Shapes and Patterns: The Phenomenology of Modulated Phases. *Science ()* 267, 476–483 (1995).) 267, 476–483 (1995). (1979).
15. Tsukahara, H., Iwano, K., Mitsumata, C., Ishikawa, T. & Ono, K. Micromagnetic simulation for the magnetization reversal process of Nd-Fe-B hot-deformed nanocrystalline permanent magnets. *AIP Adv* **7**, (2017).
16. Lau, J. W., Beleggia, M. & Zhu, Y. Common reversal mechanisms and correlation between transient domain States and field sweep rate in patterned permalloy structures. *J Appl. Phys* **102**, (2007).
17. Tsukahara, H., Iwano, K., Ishikawa, T., Mitsumata, C. & Ono, K. Large-Scale micromagnetics simulation of magnetization dynamics in a permanent magnet during the initial magnetization process. *Phys. Rev. Appl.* **11**, 014010 (2019).
18. Lee, S. J., Sato, S., Yanagihara, H., Kita, E. & Mitsumata, C. Numerical simulation of random magnetic anisotropy with solid magnetization grains. *J. Magn. Magn. Mater.* **323**, 28–31 (2011).
19. Mitsumata, C. & Kotsugi, M. Interpretation of Kronmüller formula using Ginzburg-Landau theory. *J. Magnetics Soc. Japan.* **46**, 2209R001 (2022).
20. Badea, R. & Berezovsky, J. Mapping the landscape of Domain-Wall pinning in ferromagnetic films using differential Magneto-Optical microscopy. *Phys. Rev. Appl.* **5**, 064003 (2016).
21. Cherifi, S. et al. Virgin domain structures in mesoscopic Co patterns: comparison between simulation and experiment. *J Appl. Phys* **98**, (2005).
22. Rave, W. & Hubert, A. Magnetic ground state of a thin-film element. *IEEE Trans. Magn.* **36**, 3886–3899 (2000).
23. Zapperi, S., Cizeau, P., Durin, G. & Stanley, H. E. Dynamics of a ferromagnetic domain wall: Avalanches, depinning transition, and the Barkhausen effect. *Phys. Rev. B.* **58**, 6353–6366 (1998).
24. Parkin, S. S. P., Hayashi, M. & Thomas, L. Magnetic Domain-Wall racetrack memory. *Sci. (1979).* **320**, 190–194 (2008).
25. Chappert, C., Fert, A. & Van Dau, F. N. The emergence of spin electronics in data storage. *Nat. Mater.* **6**, 813–823 (2007).
26. Rahm, M., Stahl, J., Wegscheider, W. & Weiss, D. Multistable switching due to magnetic vortices pinned at artificial pinning sites. *Appl. Phys. Lett.* **85**, 1553–1555 (2004).
27. Kläui, M. et al. Domain wall pinning in narrow ferromagnetic ring structures probed by magnetoresistance measurements. *Phys. Rev. Lett.* **90**, 097202 (2003).
28. Punz, D. et al. Theory and micromagnetics of pinning mechanism at cylindrical defects in perpendicular magnetic films. *J Appl. Phys* **107**, (2010).
29. Chang, C. R. & Yang, J. S. The effect of structural defects on magnetic switching in thin ferromagnetic patterned films. *IEEE Trans. Magn.* **43**, 923–926 (2007).
30. Burgess, J. A. J. et al. Quantitative Magneto-Mechanical detection and control of the Barkhausen effect. *Sci. (1979).* **339**, 1051–1054 (2013).
31. Ibrahim, N. B., Edwards, C. & Palmer, S. B. Pulsed laser ablation deposition of yttrium iron Garnet and cerium-substituted YIG films. *J. Magn. Magn. Mater.* **220**, 183–194 (2000).
32. Schmidt, F. & Hubert, A. Domain observations on CoCr-layers with a digitally enhanced Kerr-microscope. *J. Magn. Magn. Mater.* **61**, 307–320 (1986).
33. Niyaifar, M., Mohammadpour, H. & Behmanesh, A. Correlation of structural distortion with magnetic properties of Pr-YIG system. *J. Alloys Compd.* **683**, 495–500 (2016).

34. Sekiyama, A. et al. Itinerant bulk 4f character of strongly valence-fluctuating CeRu2 observed by high-resolution Ce 3d–4f resonance photoemission. *Solid State Commun.* **121**, 561–564 (2002).
35. Iwasaki, T. et al. Bulk and surface electronic structures of $\mathrm{CePd}X$ $(X = \mathrm{As}, \mathrm{Sb})$ studied by $3d - 4f$ resonance photoemission. *Phys Rev B* 61, 4621–4628 (2000).
36. Yang, Z., Lange, M., Volodin, A., Szymczak, R. & Moshchalkov, V. V. Domain-wall superconductivity in superconductor–ferromagnet hybrids. *Nat. Mater.* **3**, 793–798 (2004).
37. Nishio, T. et al. High-throughput analysis of magnetic phase transition by combining table-top sputtering, photoemission electron microscopy, and Landau theory. *Sci. Technol. Adv. Materials: Methods*. **2**, 345–354 (2022).
38. Stöhr, J. et al. Element-Specific magnetic microscopy with circularly polarized X-rays. *Sci. (1979)*. **259**, 658–661 (1993).
39. Kotsugi, M. et al. Novel magnetic domain structure in iron meteorite induced by the presence of L1 $_0$ -FeNi. *Appl. Phys. Express*. **3**, 013001 (2010).
40. Streubel, R. et al. Retrieving spin textures on curved magnetic thin films with full-field soft X-ray microscopies. *Nat. Commun.* **6**, 7612 (2015).
41. Hierro-Rodriguez, A. et al. Revealing 3D magnetization of thin films with soft X-ray tomography: magnetic singularities and topological charges. *Nat. Commun.* **11**, 6382 (2020).
42. Gilbert, D. A. et al. Structural and magnetic depth profiles of magneto-ionic heterostructures beyond the interface limit. *Nat. Commun.* **7**, 12264 (2016).
43. Shi, J., Tehrani, S. & Scheinfein, M. R. Geometry dependence of magnetization vortices in patterned submicron NiFe elements. *Appl. Phys. Lett.* **76**, 2588–2590 (2000).
44. Ohtsuki, T. et al. Magnetic domain observation of FeCo thin films fabricated by alternate monoatomic layer deposition. *J. Appl. Phys.* **115**, 043908 (2014).
45. Ohkochi, T. et al. Investigation of deterministic and cumulative nature in helicity-dependent optical switching of ferrimagnetic Gd–Fe–Co films. *J. Magn. Magn. Mater.* **593**, 171854 (2024).
46. Yamamoto, S. et al. Element Selectivity in Second-Harmonic Generation of <msub><mrow><mi>GaFeO <mrow><mn>3 by a Soft-X-Ray Free-Electron Laser. *Phys Rev Lett* 120, 223902 (2018).
47. Kunii, S., Masuzawa, K., Fogiatto, A. L., Mitsumata, C. & Kotsugi, M. Causal analysis and visualization of magnetization reversal using feature extended Landau free energy. *Sci. Rep.* **12**, 19892 (2022).
48. Foggiatto, A. L., Kunii, S., Mitsumata, C. & Kotsugi, M. Feature extended energy landscape model for interpreting coercivity mechanism. *Commun. Phys.* **5**, 277 (2022).
49. Obayashi, I., Hiraoka, Y. & Kimura, M. Persistence diagrams with linear machine learning models. *J. Appl. Comput. Topol.* **1**, 421–449 (2018).
50. Kunii, S., Foggiatto, A. L., Mitsumata, C. & Kotsugi, M. Super-hierarchical and explanatory analysis of magnetization reversal process using topological data analysis. *Sci. Technol. Adv. Materials: Methods*. **2**, 445–459 (2022).
51. Foggiatto, A. L. et al. Visualization of the magnetostriction mechanism in Fe-Ga alloy single crystal using dimensionality reduction techniques. *IEEE Trans. Magn.* **59**, 1–4 (2023).
52. Taniwaki, M. et al. Analysis of Magnetization Reversal Process of Non-Oriented Electromagnetic Steel Sheet by Extended Landau Free Energy Model. in. *IEEE International Magnetic Conference - Short Papers (INTERMAG Short Papers)* 1–2 (IEEE, 2023). (2023). https://doi.org/10.1109/INTERMAGShortPapers58606.2023.10228817
53. Mitsumata, C., Foggiatto, A. L., Kotsugi, M. A. & Data-Driven Extended Landau Theory Method for the Coercivity Analysis of Magnetic Materials. in *IEEE International Magnetic Conference - Short papers (INTERMAG Short papers)* 1–2 (IEEE, 2024). 1–2 (IEEE, 2024). (2024). https://doi.org/10.1109/INTERMAGShortPapers61879.2024.10576907
54. Hirata, A., Wada, T., Obayashi, I. & Hiraoka, Y. Structural changes during glass formation extracted by computational homology with machine learning. *Commun. Mater.* **1**, 98 (2020).
55. Hiraoka, Y. et al. Hierarchical structures of amorphous solids characterized by persistent homology. *Proc. Natl. Acad. Sci.* **113**, 7035–7040 (2016).
56. Edelsbrunner, L. Zomorodian. Topological persistence and simplification. *Discrete Comput. Geom.* **28**, 511–533 (2002).
57. Obayashi, I., Nakamura, T. & Hiraoka, Y. Persistent homology analysis for materials research and persistent homology software: HomCloud. *J Phys. Soc. Japan* **91**, (2022).
58. Kimura, M., Obayashi, I., Takeichi, Y., Murao, R. & Hiraoka, Y. Non-empirical identification of trigger sites in heterogeneous processes using persistent homology. *Sci. Rep.* **8**, 3553 (2018).
59. Minamitani, E., Obayashi, I., Shimizu, K. & Watanabe, S. Persistent homology-based descriptor for machine-learning potential of amorphous structures. *J Chem. Phys* **159**, (2023).
60. Nagaoka, R. et al. Quantification of the coercivity factor in soft magnetic materials at different frequencies using topological data analysis. *IEEE Trans. Magn.* **60**, 1–5 (2024).
61. Foggiatto, A. L. et al. Analysis of the excess loss in High-Frequency magnetization process through machine learning and topological data analysis. *IEEE Trans. Magn.* **60**, 1–5 (2024).
62. Jolliffe, I. Principal component analysis. in International Encyclopedia of Statistical Science 1094–1096 (Springer Berlin Heidelberg, Berlin, Heidelberg, doi:https://doi.org/10.1007/978-3-642-04898-2_455. (2011).
63. Taniwaki, M. et al. Automated identification of the origin of energy loss in nonoriented electrical steel by feature extended Ginzburg–Landau free energy framework. *Sci. Rep.* **15**, 23758 (2025).
64. Tone, M. et al. Linking structure and process in dendritic growth using persistent homology with energy analysis. *Science Technol. Adv. Materials: Methods* **5**, (2025).

Acknowledgements

We thank Prof. H. Tabata, Prof. K. Akagi, Prof. T. Nakamura and Prof. K. Ono for useful discussions. We gratefully acknowledge Prof. H. Fukuyama for his thoughtful discussions and expert guidance, which have been instrumental in shaping the direction and depth of this study.

Author contributions

M. K. designed the project and directed the experiments and data analysis. K. M. carried out the experiments and developed the data analysis framework. A. L. F., S. K., R. N., M. T., T. Y. and C. M. supported the experiments and data analysis. I. O. and Y. H. supported the persistent homology analysis. All the authors discussed the results and contributed to the final manuscript.

Funding

This work was supported by a Japan Society for the Promotion of Science (KAKENHI) Grant-in-Aid for Scientific Research (A) (21H04656). This work was partially supported by JST-CREST (Grant No. JPMJCR21O1). C. M. is supported by Tsukuba Research Center for Energy Materials Science (TREMS), University of Tsukuba.

Declarations

Competing interests
The authors declare no competing interests.

Additional information
Supplementary Information The online version contains supplementary material available at https://doi.org/10.1038/s41598-026-39617-x.

Correspondence and requests for materials should be addressed to M.K.

Reprints and permissions information is available at www.nature.com/reprints.

Publisher's note Springer Nature remains neutral with regard to jurisdictional claims in published maps and institutional affiliations.